Proceedings of The Thirteenth (2003) International Offshore and Polar Engineering Conference
Honolulu, Hawaii, USA, May 25−30, 2003

ISBN 1−880653-60−5 (Set); ISSN 1098−6189 (Set)

Numerical Modeling and Experiments of Wave Shoaling over Semi-buried Cylinders in Sandy Bottom

Stéphan T. Grilli[1], *Sergey I. Voropayev*[2], *Firat Y. Testik*[2], *and H. Joe S. Fernando*[2]
1. Department of Ocean Engineering, University of Rhode Island, Narragansett, RI, USA
2. Environmental Fluid Dynamics Program, Arizona State University (ASU), Tempe, AZ, USA

ABSTRACT

In this paper, we study the propagation of long periodic waves over semi-buried cylindrical objects in the bottom. We present a combination of laboratory wave tank experiments, with a sandy bottom, and numerical modeling, using a two-dimensional fully nonlinear potential flow model. Experiments provide wave elevation at gages and velocity fields measured around the semi-buried objects, using an Acoustic Doppler Velocimetry (ADV) method. The model is run for the same geometry and wave parameters as in the experiments. A numerical absorbing beach is used to both prevent waves from overturning and specify wave absorption in the model surfzone. Bottom friction in the shoaling region is specified as a corresponding energy loss in the model, by using an absorbing surface pressure. Without the semi-buried cylinder, the comparison between computed and experimental results is quite good for both surface elevation and near bottom velocities, even for waves near the breaking point. With the cylinder, the agreement of computed and measured velocities close to the cylinder is also good, except, just in front and behind the cylinder, likely due to vortex shedding. The model can thus be used to accurately provide background wave fields around the buried object, say, at one diameter away. Based on these, more refined hydrodynamic and sediment transport modeling can be performed in future studies.

KEYWORDS : Nonlinear nearshore wave transformations, wave shoaling and breaking, numerical wave tank, boundary element method, moving bottom, sediment transport.

INTRODUCTION

The motivation for this work is the recent interest of the U.S. Navy for the behavior, and possible scour/burial, of large cylindrical objects (mines) on the ocean bottom, in a coastal environment where nonlinear waves play the dominant role.

The behavior of solid objects, such as mines, located on or partly within sandy bottom, in shallow water coastal areas, is strongly affected by the near bottom velocity and pressure induced by shoaling water waves. In turn, such objects also strongly affect the near bed wave flow, usually making velocities increase near the objects and thus increasing local sediment transport rates (Voropayev et al., 2002a). Predicting the objects' burial or scouring thus requires a detailed analysis of near bottom wave fields around the object. Long shoaling waves (swells) approaching breaking in sandy coastal areas usually become locally two-dimensional (2D) (in a vertical plane), due to refraction. Such waves, when propagating over sandy bottom in shallow water also usually induce the formation of ripples. As waves shoal up, their increasing nonlinearity leads to both up-down and front-rear asymmetry of the wave profile, and to a corresponding asymmetry of the near bottom velocities. Such asymmetry in wave forcing, in turn induces an asymmetry of the induced sediment transport, causing ripples to migrate up slope (Vittori and Blondeaux, 1990; Blondeaux et al., 2000). Numerical modeling of such phenomena, particularly in the presence of objects on the bottom is a very challenging problem, for which little has been reported (Kan et al., 2001). More experimental work has been reported, mostly for 2D configurations, such as waves propagating over pipelines (Cevik and Yuksel, 1999). Voropayev et al. (2002a), however, studied the burial/scouring of short cylindrical horizontal objects, under a shoaling swell, a case for which sediment transport is three-dimensional (3D), but the forcing flow, except close to the object, is essentially 2D.

The present modeling work was performed in parallel with the latter experimental work. A Numerical Wave Tank (NWT) solving fully nonlinear potential flow equations was used (Grilli and Sub-

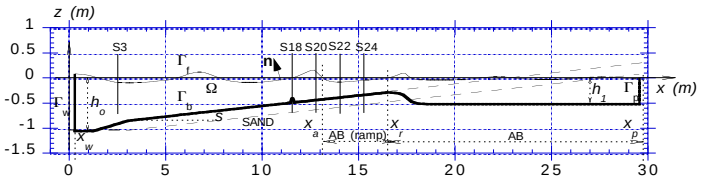

Fig. 1 : Sketch of NWT set-up for ASU's laboratory tank, for periodic wave shoaling and breaking computations over a sandy slope $s = 1 : 24$. Note, AB: absorbing beach for $x \geq x_a$; piston wavemaker at $x = x_w$. (— —) indicates the position of the sand layer in the actual wave tank at ASU.

ramanya, 1996; Grilli and Horrillo, 1987). This model has been extensively experimentally validated, and shown to accurately simulate shoaling of waves over mildly sloping beaches (including barred beaches), up to the breaking point (Grilli et al., 1994, 1997a, Grilli and Horrillo, 1997b,1999). Here, the NWT was set-up and run for the same geometry and wave parameters as in the experiments performed at Arizona State University (ASU; see Voropayev et al. 2002a,b, for details of the experimental set-up and results). Experiments provided wave elevation at gages and velocities measured at various sections along the slope, and around semi-buried cylinders, using an Acoustic Doppler Velocimetry (ADV) method. Both wave elevation at numerical gages and velocity and pressure fields in the presence of cylindrical objects were computed in the NWT. Numerical results were compared with experiments.

In the following, we briefly present model equations and numerical methods. We then give detailed results of computations and make the comparisons with experiments.

THE NUMERICAL WAVE TANK

Governing equations and boundary conditions

Equations for the two-dimensional NWT are briefly presented in the following (Grilli and Subramanya, 1996; Grilli and Horrillo, 1997a). The velocity potential $\phi(\boldsymbol{x}, t)$ is used to describe inviscid irrotational flows in the vertical plane (x, z) and the velocity is defined by, $\boldsymbol{u} = \nabla\phi = (u, w)$. Continuity equation in the fluid domain $\Omega(t)$ with boundary $\Gamma(t)$ is Laplace's equation for the potential (Fig. 1),

$$\nabla^2\phi = 0 \qquad \text{in } \Omega(t) \qquad (1)$$

On the free surface Γ_f, ϕ satisfies the kinematic and dynamic boundary conditions,

$$\frac{D\,\boldsymbol{R}}{D\,t} = (\frac{\partial}{\partial t} + \boldsymbol{u}\cdot\nabla)\,\boldsymbol{R} = \boldsymbol{u} = \nabla\phi \qquad \text{on } \Gamma_f(t) \qquad (2)$$

$$\frac{D\phi}{Dt} = -gz + \frac{1}{2}\nabla\phi\cdot\nabla\phi - \frac{p_f}{\rho} \qquad \text{on } \Gamma_f(t) \qquad (3)$$

respectively, with $\boldsymbol{R}$, the position vector on the free surface, g the gravitational acceleration, z the vertical coordinate, p_f the free surface pressure, and ρ the water density. Along the bottom boundary Γ_b, a no-flow condition is prescribed as,

$$\overline{\frac{\partial\phi}{\partial n}} = 0 \qquad \text{on } \Gamma_b \qquad (4)$$

where the overline denotes specified values.

Various methods have been used for wave generation in this NWT. Here, periodic waves are generated on boundary Γ_w using a solid piston wavemaker, as in the experiments, moving according to a simple sinusoidal motion. Thus, for a specified wavemaker or wave motion $x = x_w(t)$ on $\Gamma_{r1}(t)$ (Fig. 1), we have,

$$\overline{x_w} = \frac{S_o}{2}\,\sin(\omega t) \;\;;\;\; \overline{\frac{\partial\phi}{\partial n}} = -\frac{\mathrm{d}x_w}{\mathrm{d}\,t} \qquad \text{on } \Gamma_w \qquad (5)$$

where overlines denote specified values, S_o and ω denote wavemaker stroke and circular frequency, respectively, and the time derivative follows the wavemaker motion. Note, in the computations, the piston motion is ramped-up over three wave periods, by modulating the stroke by a tanh function of time. See references for details.

Wave energy absorption

Following Grilli and Horrillo (1997) an absorbing beach (AB) is used in the NWT, for $x \geq x_a$ (Fig. 1), to both prevent waves from overturning and breaking at the top of the slope (which would interrupt computations) and to dissipate the energy of incident waves. In the AB, an external absorbing pressure $p_f = p_a$ is specified on the free surface, by way of the dynamic free surface condition (3) (with $z = \eta$), to create a negative work and absorb wave energy. To create additional wave reduction through de-shoaling, the bottom geometry within the AB is specified somewhat similar to a natural bar, with a depth increasing to $h = h_1$ (Fig. 1).

Here, the AB absorbing pressure is specified proportional to the normal particle velocity on the free surface,

$$p_a(x, \eta, t) = \nu_a(x)\,\frac{\partial\phi}{\partial n}(\eta(x, t)) \qquad (6)$$

in which ν_a is the beach absorption function. This function is first ramped-up from 0 to ν_{ao} and then maintained constant over the AB. We have,

$$\nu_a(x) = \nu_{ao}\,\rho\sqrt{gh_1}\;f(x) \qquad (7)$$

where ν_{ao} is a non-dimensional beach absorption coefficient, and $f(x)$ follows a tanh variation for $x_a \leq x \leq x_r$, and $f(x) = 1$ for $x_r < x \leq x_p$.

Following Grilli and Horrillo (1997), an absorbing piston (AP) is also specified at the extremity of the AB, for $x = x_p$. This AP moves proportionally to the hydrodynamic pressure force caused by waves, calculated as a function of time in the NWT. See the reference for details. Grilli and Horrillo (1997) showed that the combination AB/AP allows to absorb incident wave energy in the NWT, to within any specified small fraction.

In the present applications, we wish to simulate wave shoaling over a rippled sandy bed. Although for short distances of propagation over a smooth bottom, wave damping due to bottom friction is quite small and usually neglected in numerical models, in the present case, bed roughness due to ripples may induce more significant wave damping and bottom friction should be accounted for in the NWT. Since no mechanism is available to dissipate energy in potential flow models, the same method as used for the AB is

now used to specify energy dissipation due to bottom friction over the shoaling region of the NWT, which has the rippled sandy bed, i.e., for $x_w < x \leq x_a$ (Fig. 1). More details regarding this new addition to the NWT are given below.

The wave induced shear stress in the tangential direction s to the bottom, in turbulent conditions, is given by (e.g., Fredsoe and Deigaard, 1994),

$$\tau_{bs} = \frac{1}{2}\,\rho f_{wb}\,|u_{bs}|\,u_{bs} \quad \text{with} \quad f_{wb} = c_1\left(\frac{\zeta_{bs}}{k_l}\right)^{c_2} \tag{8}$$

where, $u_{bs} = \frac{\partial \phi}{\partial s}$ calculated on the bottom, is the tangential velocity on the bottom, $c_1 \simeq 0.04$ and $c_2 \simeq -0.25$ are constant coefficients, $k_l \simeq 2.5\,d_{50}$ is the bed roughness, with d_{50} the median diameter for the sediment, and ζ_{bs} is the maximum excursion of water particles on the bottom. For linear waves, the latter can be found as $\zeta_{bs} = u_{bs}^{max}/\omega$, where u_{bs}^{max} denotes the maximum tangential velocity on the bottom at any given x location. For nonlinear waves, however, this value must be calculated based on local wave parameters.

The energy flux dissipated due to bottom friction over the shoaling zone is given by the work of the shear stress per unit time,

$$E_{fd} = \frac{1}{2}\,\rho \int_{x_w}^{x_r} f_{wb}\,|u_{bs}|\,u_{bs}^2\,\mathrm{d}s \tag{9}$$

The corresponding absorbing pressure is defined on the free surface as,

$$p_b = \nu_{bo}\; f_{wf}(x)\,\rho u_{bs}^2\,\mathrm{sign}(\frac{\partial \phi}{\partial n}) \;\; ; \text{on } \Gamma_f,\; x_w < x \leq x_r \tag{10}$$

with $u_{bs} = \frac{\partial \phi}{\partial s}$ calculated on the free surface, and $f_{wf}(x)$ is interpolated at x from values of f_{wb} calculated on the bottom. By equating the work per unit time of this pressure over the free surface and E_{fd}, we find,

$$\nu_{bo} = E_{fd}/\{\rho \int_{x_w}^{x_r} f_{wf}\,u_{bs}^2\,|\frac{\partial \phi}{\partial n}|\,\mathrm{d}s\} \tag{11}$$

a non-dimensional bottom friction dissipation coefficient, from which we can calculate the absorbing pressure over the shoaling zone using Eq. (10), and specify it in the model dynamic free surface boundary condition (3) as $p_f = p_b$.

In the NWT, $\zeta_{bs}(x)$ values in Eq. (8) are initialized based on linear shoaling wave theory as,

$$\zeta_{bs} = \frac{H_o}{2\,\cos\theta\,\sinh kh}\sqrt{\frac{n_o}{n}} \tag{12}$$

where θ is the slope angle, $h(x)$ denotes the local depth, k is given by the linear dispersion relationship, as a function of h and ω, and n as a function of kh (with $n_o = n(k_o h_o)$) as,

$$\frac{\omega^2}{g} = k\,\tanh kh \;\; ; \quad n = \tanh kh\left(1 + \frac{2kh}{\sinh 2kh}\right) \tag{13}$$

respectively, with H_o the incident wave height in depth h_o, estimated using linear wavemaker theory for a piston wavemaker as,

$$H_o = 2S_o\,\frac{\cosh 2kh\; -\; 1}{2kh\; +\; \sinh 2kh} \tag{14}$$

where S_o denotes the wavemaker stroke. After the initial ramp-up period, ζ_{bs} values are updated at each time step using computed values of u_{bs}^{max}.

Numerical model

In the NWT, Eq. (1) is transformed into a Boundary Integral Equation (BIE), using Green's 2nd identity, and solved by a Boundary Element Method (BEM). The BIE is expressed for N discretization nodes on the boundary, and M higher-order elements are defined to interpolate in between discretization nodes. In the present applications, quadratic isoparametric elements are used on lateral and bottom boundaries, and cubic elements ensuring continuity of the boundary slope are used on the free surface. In these elements, referred to as Mid Cubic Interpolation (MII) elements, both geometry and field variables are interpolated between each pair of nodes, using the mid-section of a four-node "sliding" isoparametric element. Detailed expressions of BEM integrals (regular, singular, quasi-singular) are given in Grilli and Subramanya (1996), for both isoparametric and MII elements.

Free surface boundary conditions (2) and (3) are time integrated based on two second-order Taylor series expansions expressed in terms of a time step Δt and of the Lagrangian time derivative, D/Dt, for ϕ and $\boldsymbol{R}$. First-order coefficients in the series correspond to free surface conditions (2) and (3), in which ϕ and $\partial\phi/\partial n$ are obtained from the BEM solution of the BIE for $(\phi,\, \partial\phi/\partial n)$ at time t. Second-order coefficients are expressed as D/Dt of Eqs. (2) and (3), and are calculated using the solution of a second BIE for $(\partial\phi/\partial t,\, \partial^2\phi/\partial t\partial n)$, for which boundary conditions are obtained from the solution of the first BIE and the time derivative of Eqs. (3) to (5). Detailed expressions for the Taylor series can be found in Grilli et al. (1989).

At each time step, global accuracy of computations is verified by computing errors in total volume and energy for the generated wave train. Earlier work showed that these errors are function of both the size (i.e., distance between nodes) and the degree (i.e., quadratic, cubic,...) of boundary elements used in the spatial discretization, and of the size of the selected time step. Thus, Grilli and Subramanya (1996) adaptively selecting the optimal time step, based on a mesh Courant number $\mathcal{C}_o(t)$ and, for MII elements, showed that the optimum value of $\mathcal{C}_o$ was about 0.45. This value is used in the present applications.

In computations involving finite amplitude waves, mean drift currents occur ("Stokes drift"), which continuously move free surface discretization nodes/Lagrangian markers away from the wavemaker into the NWT. Grilli and Subramanya (1996) developed regridding methods in which nodes can be redistributed at constant arclength intervals over specified regions of the free surface. This method is used here over the whole free surface, every 10 time steps.

APPLICATIONS

Modeling of ASU's tank in the NWT

Fig. 1 shows a sketch of the computational domain defined

in the NWT to simulate laboratory experiments in ASU's wave tank. A piston wavemaker is specified on the leftward boundary at $x = x_w$, with initial (mean position) at $x = 0$. The initial water depth is $h_o = 1.05$ m.

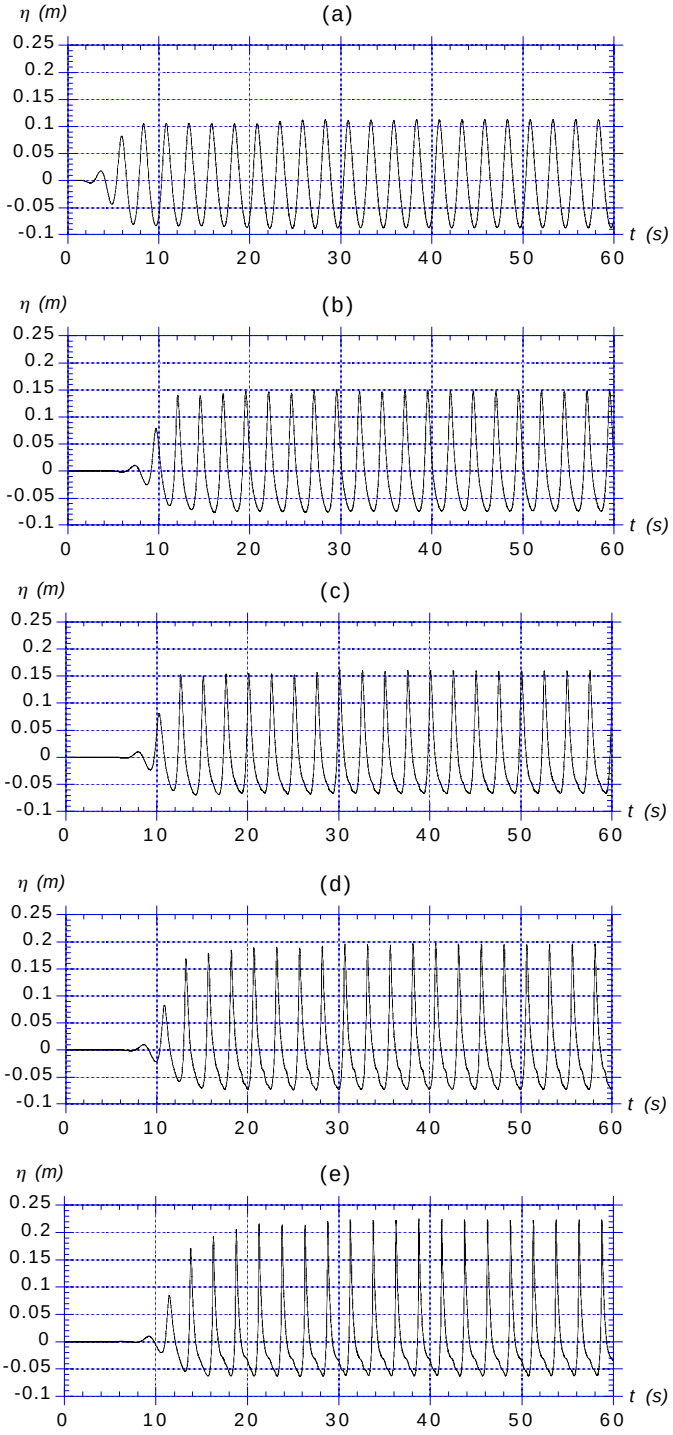

Fig. 2 (no obstacle) : Instantaneous surface elevations computed at gages (no obstacle) : (a) S3 ($x = 2.438$ m); (b) S18 ($x = 11.583$ m); (c) S20 ($x = 12.802$ m); (d) S22 ($x = 14.021$ m); (e) S24 ($x = 15.240$ m), in the tank of Fig. 1 (without the bottom obstacle), for periodic waves shoaling over sandy bottom, with $H_o = 0.206$ m and $T = 2.5$ s.

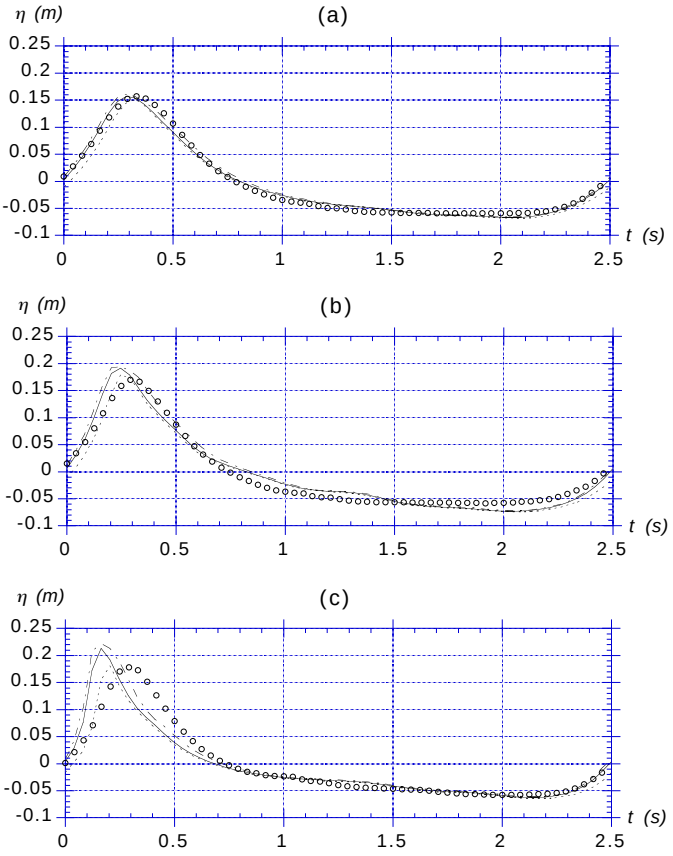

Fig. 3 (no obstacle) : Phase-averaged (20 periods) surface elevations at gages (no obstacle) : (a) S20; (b) S22; (c) S24, for the same case as in Fig. 2. With : computed (——) average; (- - - -) minimum; (—- -—) maximum; measured average (○), elevations.

On the bottom, the tank has a 0.21 m thick layer of fine sand with $d_{50} = 0.06$ cm (located between the large chained lines on Fig. 1), starting at $x = 1.219$, with a 1:6 slope, and followed, at $x = 3.048$, by a 1:24 slope.

As detailed above, in the NWT, the surfzone is modeled by an AB, starting, here, at $x_a = 12.8$ m. In the AB, the sloping bottom is interrupted at $x_r = 16.5$, slightly before the breaking point in the experiments and, for $x > x_r$, the depth is gradually increased to $h_1 = 0.5$ m, following a gentle tanh variation. The AB non-dimensional absorption coefficient ν_{ao} is ramped up from 0 to 0.4 from x_a to x_r, and then maintained constant.

In the laboratory tank, the sandy bottom is rectified before each new experiments. However, it is observed that sand ripples rapidly form under wave action. Measurements are made after the bed shape is fully developed. In the NWT, we did not represent the exact shape of ripples, as this would not affect shoaling waves very much. However, the effect of ripples is represented by a dissipation corresponding to bottom friction. Thus, we specify the surface absorbing pressure and calculate ν_{bo} as detailed above, using Eq. (11), for $x = 1.219$ m to x_r. For the bottom friction coefficient f_{wb} in Eqs. (8) to (11), we use $c_2 = -0.25$. For c_1, however, after running several calibration tests, we found it necessary to specify a larger value, 0.25, than the typical value used for a smoother bottom. This is likely due to the effect of

ripples, which may increase bottom friction effects on waves.

Some experiments in ASU's tank were run without any bottom obstacles. In other experiments, a circular cylinder of radius $r = 0.084$ m, and length equal to almost the tank width, was placed on the bottom at $x = 11.583$ m, hereafter referred to as section 18 (or S18; Fig. 1). We modeled both cases in the computational domain (Fig. 1). The BEM discretization had 342 nodes, $N_f = 149$ of which were on the free surface, thus defining 148 MII sliding cubic elements. With $x_p = 29.6$ m for $t = 0$, the initial element length on the free surface was $\Delta x_o = 0.2$ m. Quadratic 3-node isoparametric elements are used on the other parts of the boundary. There is a total of $N = 342$ nodes and $M = 243$ elements. The initial time step was $\Delta t_o = 0.034$ s, which is consistent with a Courant number equal to 0.45.

Calibration and validation of NWT

Experiments were run with and without the cylindrical bottom obstacle, and measurements of surface elevation and velocity were taken and (phase) averaged, in the second case when the cylinder was half-buried. We run similar cases in the NWT and found that the cylinder had very little effect on computed phase-averaged wave elevations, even right above the cylinder (Fig. 4). Velocities, however, particularly closer to the cylinder were strongly affected by its presence.

Hence, the first step of calibration of the incident wave in the NWT was carried out using measurements made at gages without the cylinder in place on the bottom, and running computations for a plane sandy slope. All cases were run for a wave period $T = 2\pi/\omega = 2.5$ s and an experimental wavemaker stroke $S_o = 0.25$ m (Eq. (8)). When comparing measured and computed waves at the toe of the slope (S3 in Fig. 1), however, it was found that computed waves were too large. This was later explained by observing that there were significant water leaks on the wavemaker sides and bottom in ASU's experiments, hence, leading to a reduced wavemaking efficiency. We found that measured waves could accurately be reproduced at gage S3 in the NWT, by simply reducing the piston stroke to $S_o = 0.21$ m. Doing so, we obtained at S3 a wave height (phase-averaged over 20 periods) $H_o = 0.206$ m, as compared with $H_o = 0.210$ m in the experiments.

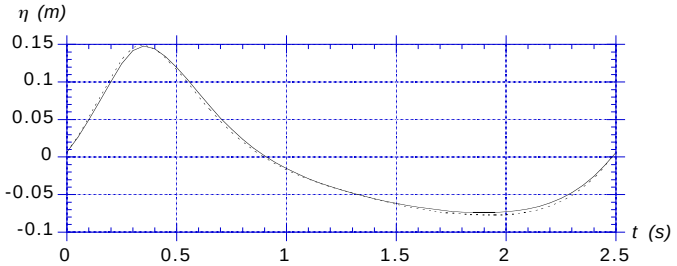

Fig. 4 : Phase-averaged free surface elevation computed at gage S18 : (——) without obstacle; (- - - -) with obstacle. Wave case of Fig. 2.

A total of 3500 time steps were usually run in each of these computations (the CPU time per time step was about 0.75 s on a MAC-G4/500MHz), which led to a maximum simulated time of 75.8 s and an average time step about 0.02s. This also corresponded to about 30 incident wave periods. In the computations, the relative error on the NWT conservation of mass flux through the boundary at each time step was less than $4\,10^{-5}$%, and for total NWT volume, the error was less than 0.45% at the end of the computations. Part of this, however, is due to some water exiting the domain through the AP motion, by way of nonlinear effects.

Due to the ramp-up of the wavemaker motion and delays due to wave propagation over the slope, the first 5-10 periods or so in the computations were usually excluded from phase averaging of results over one wave period, for comparison with experimental results. Hence, in the computations, time averages were typically performed over 20 periods or so, when waves had reached a quasi-steady state in the NWT. By contrast, in the experiments, time averages were performed over 30-40 wave periods.

Fig. 2 shows instantaneous wave elevations computed at gages S3 to S24 (Fig. 1), for the sandy bottom without the cylindrical obstacle. The increasing wave nonlinearity during shoaling induces both increasing up/down and front/rear asymmetry of the wave shape.

Fig. 3 shows averages of Figs 2(c) to (e) results, over 20 wave periods, as well as computed minimum and maximum envelopes. Average values are compared to experimental results. The agreement is quite good for results at gages S20 and S22, but less good for S24, particularly for the wave shape near the crest. This is likely due to the use of an empirical AB in the present computations to model such nearly breaking waves. More accurate results for breaker shape and height could be obtained by using the spilling breaker model of Guignard and Grilli (2001). We elected, however, not to tackle such more computationally intensive computations, which would have unnecessarily burdened our effort here, since the focus was not on surfzone waves. Anyway, discrepancies at gage S24 will not affect results at section S18, which is downslope of S20 where the agreement between numerical and experimental results is very good. The cylindrical obstacle will be located next in section S18.

In this respect, Fig. 4 shows average wave elevation computed at gage S18, with and without the bottom obstacle. The effect of the obstacle is quite small and translates into a 6% maximum change in wave elevation.

Fig. 5 shows horizontal and vertical velocities computed in sections S20, S22 and S24, at 0.1 m above the bottom without the obstacle, and phase-averaged over 20 periods. The horizontal velocity is compared with ADV measurements. The agreement is quite good, even at section S24. Hence, errors on wave crest shape (Fig. 3c) do not seem to affect predicted near bottom velocities to the same extent. Comparing Figs. 3 and 5, we see that horizontal velocities directly reflect wave asymmetry with, as expected, larger onshore velocities under crests and smaller offshore velocities under troughs. Vertical velocities are out of phase with horizontal velocities and also strongly asymmetric, with much larger upward velocities, preceding crests, than downward velocities, preceding troughs. Such velocity patterns are directly related to observed sediment transport (migrating ripples; Voropayev et al., 2002b).

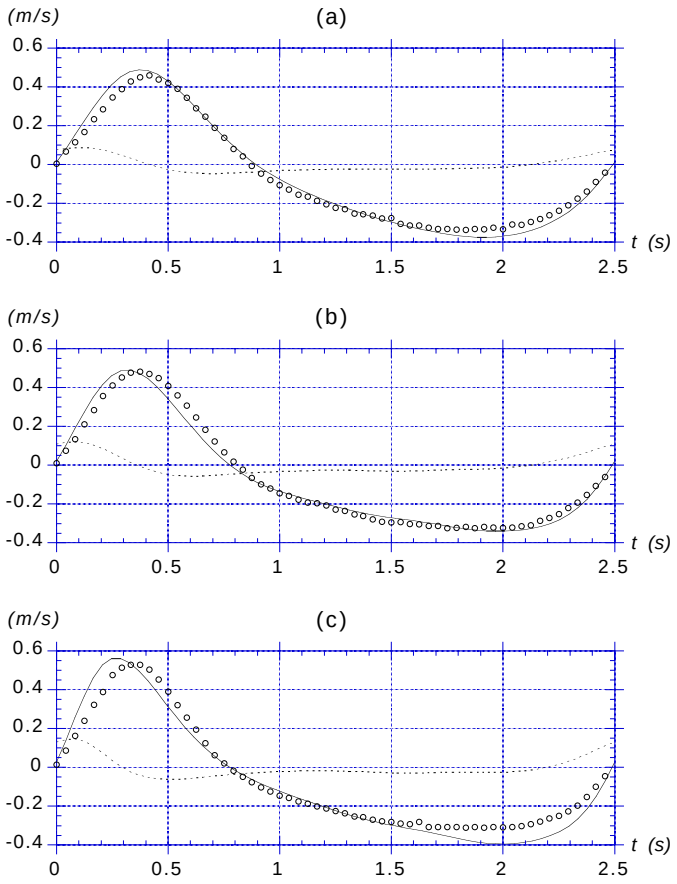

Fig. 5 (no obstacle) : Phase-averaged (20 periods) particle velocities at gages (at $z = -h + 0.1$): (a) S20; (b) S22; (c) S24, for the same cases as in Figs. 2,3. With : computed average (——) u and (- - - -) w velocities; measured average ($\circ$) u velocity.

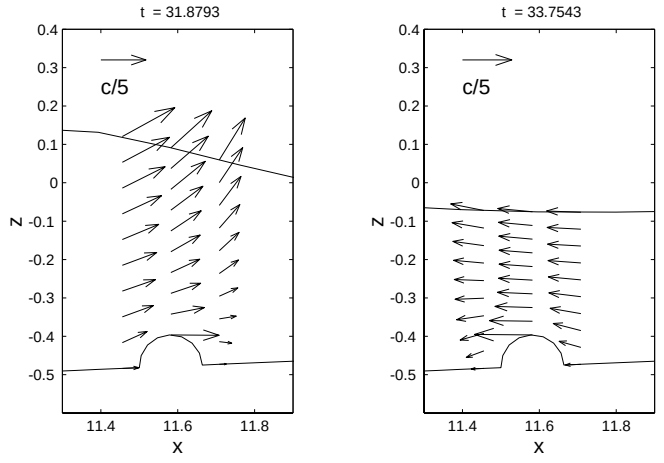

Fig. 6 (with cylindrical obstacle; Fig. 1) : Instantaneous velocity vectors at time $t = 31.88$ and 33.75 s, above the obstacle at section S18, for wave case of Fig. 2. Incident wave speed in deep water is $c_o = gT/(2\pi) = 3.9$ m/s. Local wave celerity is about $c = 2.6$ m/s.

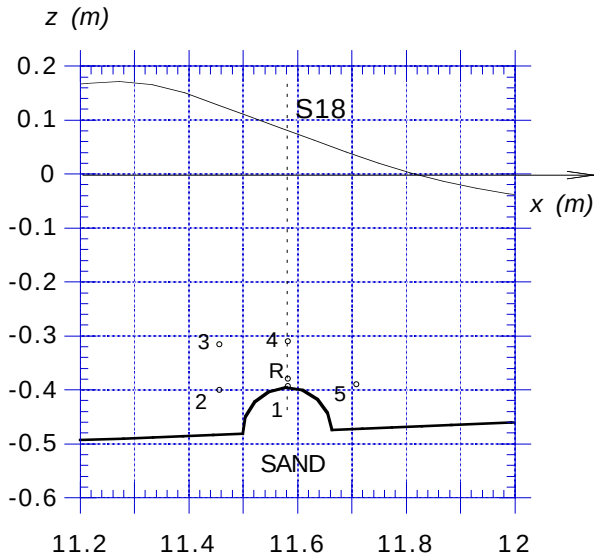

Fig. 7 : Locations for computations of phase-averaged velocities at points 1-5 around the obstacle, at section S18. Same wave case as Fig. 6. R is reference point (no obstacle).

Velocity field around cylindrical obstacle

Computations are repeated with the cylindrical obstacle semi-buried on the bottom of section S18 (Fig. 1). Wave and NWT parameters are similar to those used above.

As shown in Fig. 4, free surface elevations are not significantly affected by the presence of the cylinder. Hence, the NWT validation discussed above also applies to this case. Internal velocities, both instantaneous and phase-averaged, are computed at points around the obstacle and compared to experiments, to illustrate the effect of the obstacle on the flow and, possibly, on induced sediment transport.

Fig. 6 shows two typical views of instantaneous velocity vectors computed above and near the cylindrical obstacle, when a wave crest is about to pass over it ($t = 31.88$ s) and a wave trough has just passed by ($t = 33.75$ s). Incident waves are fairly long at this location, with a ratio of length over depth larger than 16. In the leftward figure, both in front and behind the cylinder, we see markedly larger horizontal velocities u near the free surface than closer to the bottom. For such long waves, this is clearly due to the large nonlinearity (wave height is about 50% the local depth and maximum particle velocities at the surface reach about 0.7 m/s or about 27% the local wave celerity $c = 2.6$ m/s). In the rightward figure, u is fairly uniform over depth away from the cylinder, as expected for a long wave. Moving closer to the obstacle, we see in both figures a large increase in $u$right above the cylinder. This could be expected from simple potential flow computations of a circular cylinder in a uniform flow, which would predict u on the cylinder top, up to twice the free stream velocity. On the sides, we also see the effect of the cylinder on vertical velocities w, with the flow being forced to follow the cylinder boundary and thus being forced upward on the upstream side, and downward on the downstream side, with respect to the flow direction (i.e., sign of u).

Fig. 7 shows locations for 5 points around the cylinder, where

phase-averaged velocities u and w are calculated in Figs. 8 and 9. These are compared with a reference velocity calculated at 0.1 m above the bottom in S18 without the obstacle, and with experiments (point R).

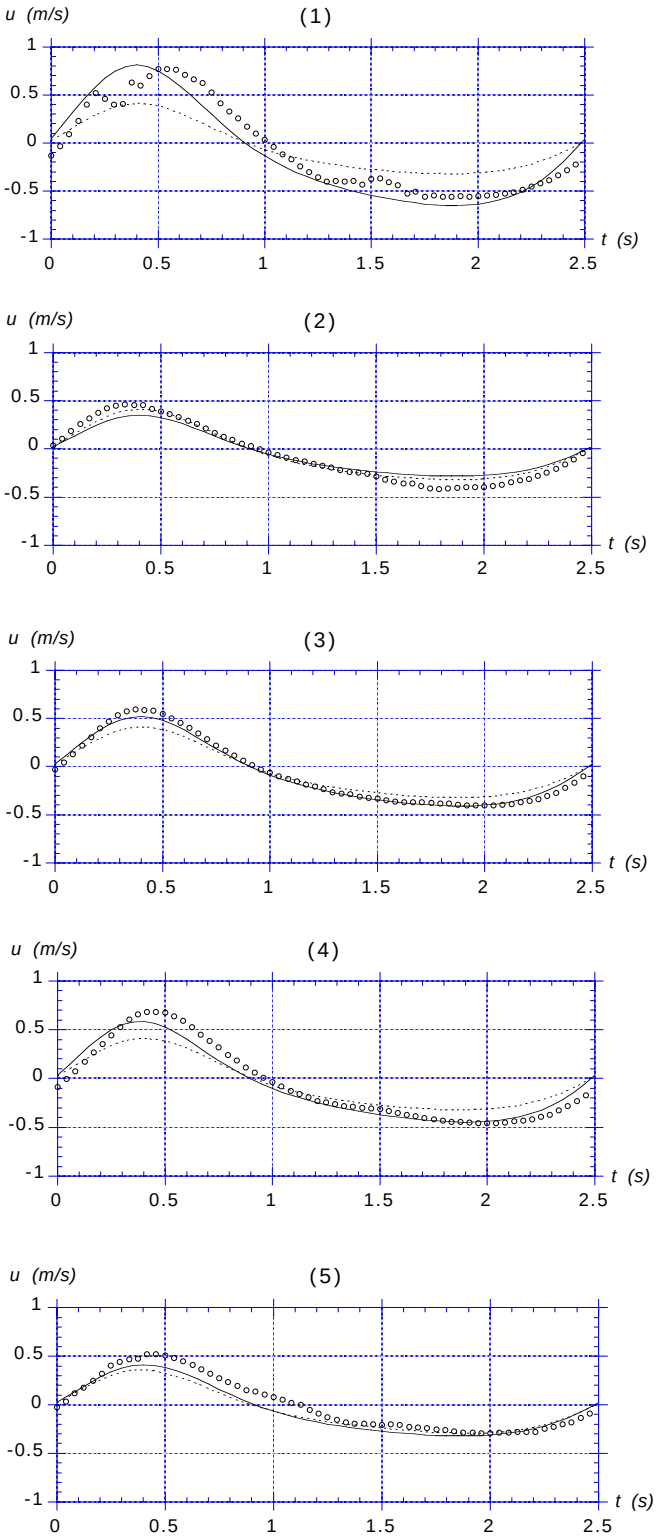

Fig. 8 : Phase-averaged horizontal velocity around the obstacle, at section S18 for points of Fig. 7. Same wave case as Fig. 6. With: (- - - - -) ref. no obstacle (R); (——) computed; (○) measured.

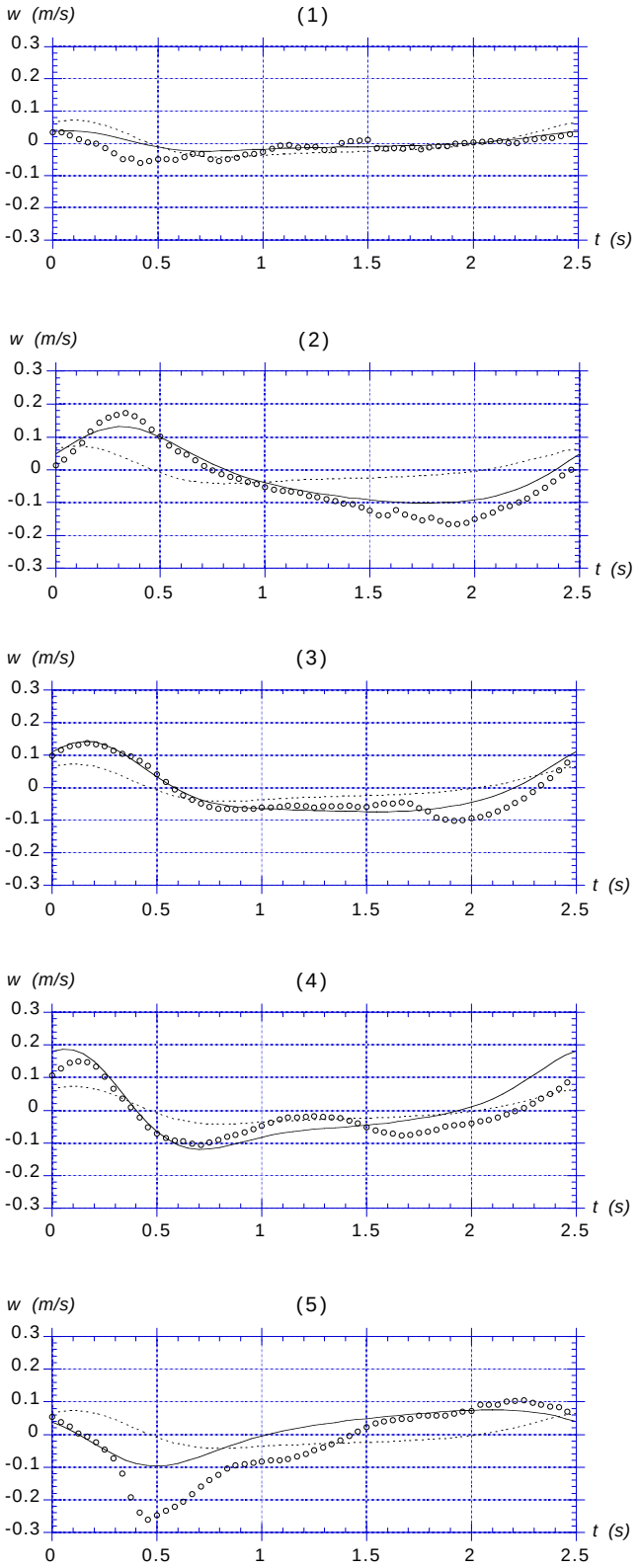

Fig. 9 : Phase-averaged vertical velocity around the obstacle, at section S18 for points of Fig. 7. Same definitions as Fig. 8.

In Figs. 8 and 9, computations of both u and w agree well with experiments for point 1 (0.001 m above the cylinder). As expected,

$|u|$ increases by a factor of 2 in both directions of the flow, as compared to results without the obstacle (R). This effect, however, is quite local as $|u|$ is not so significantly affected at points 2 and 5, one radius above the bottom and half a radius in front or behind the cylinder. As expected, w is very small at point 1 due to the no-flow condition on the cylinder. At points 3 and 4, one diameter over the bottom and one radius plus 0.001 m above the cylinder, respectively, results of computations and experiments also agree well. Here, $|u|$ increases by about 50 percent as compared to (R), and w experiences much more variations than u (and even more in experiments), due to the presence of the obstacle. At points 2 and 5, in computations, w shows the largest deviation with respect to (R), as the flow is forced to move up or down the cylinder, depending on its direction. Here, however, we see larger discrepancies between computations and experiments. These could be explained by flow separation and vortex shedding in experiments, on the downstream side of the cylinder with respect to the sign of u. Thus, at point 2, the relative increase in measured $|w|$, with respect to computations, is larger under wave troughs, when $u < 0$ and $w < 0$, and at point 5, it is larger under crests. In addition, due to the larger $|u|$ under crests (and thus vortex shedding), the increase in $|w|$ is larger at point 5 than at point 2. All of these effects should enhance sediment suspension and transport in the vicinity of the cylinder.

CONCLUSIONS

We numerically and experimentally studied the propagation of long periodic waves over semi-buried cylindrical objects in sandy bottom. After minor calibrations consisting in adjusting parameters of the absorbing beach and bottom friction dissipation, the comparison between computed and experimental results is quite good over the sandy slope, for both wave elevations and near bottom velocities, even close to breaking. [Note, the effect of bottom friction on wave shape, although enhanced by the rippled bed, only translates in the model in a few percent changes, as compared to the case without friction; hence, this is still quite a small effect.] The effect of the cylinder on wave elevation is very small. Significant changes, however, are observed for particle velocities, up to one radius away from the cylinder. Computed and measured velocities agree quite well, except for the vertical velocity in front and behind the cylinder. Measured $|w|$ increase likely due to vortex shedding, a phenomenon which is not modeled in potential flow computations. Overall, absolute velocity is increased around the cylinder, which will affect both sediment suspension and transport. This is well observed in laboratory experiments (Voropayev et al., 2002a).

Based on these results, at a short distance away from the cylinder (say $> 2r$; particularly above and upstream; see also Fig. 6), the potential flow model should accurately predict velocities. The model can thus be used to provide background wave fields around the buried object, to both study sediment transport and perform more refined modeling of the flow around the obstacle, e.g., based on solving Navier-Stokes (NS) equations and including a sediment transport model.

REFERENCES

Blondeaux, P., Foti, E. and Vittori, G. (2000) "Migrating sea ripples," *Eur. J. Mech. B, Fluids*, **19**, 285-301.

Cevik, E., Yuksel, Y. (1999) "Scour under submarine pipelines in waves in shoaling conditions," *J. Waterw., Port, Coast. Ocean Engr.*, **125**(1), 9-19.

Fredsoe, J. and Deigaard, R. (1994) *Mechanics of Coastal Sediment Transport*, Adv. Series on Ocean Engng., **3**. World Scientific Pub.

Grilli, S.T. and J. Horrillo (1997a). "Numerical generation and absorption of fully nonlinear periodic waves," *J. Engng. Mech.*, **123**(10), 1060-1069.

Grilli, S.T. and J., Horrillo (1997b). "Fully nonlinear properties of periodic waves shoaling over mild slope," *Proc. 25th Intl. Conf. on Coastal Engineering* (ICCE25, Orlando, USA, 9/96), 717-730. ASCE ed.

Grilli, S.T. and J., Horrillo (1999) "Shoaling of periodic waves over barred-beaches in a fully nonlinear numerical wave tank," *Intl. J. Offshore and Polar Engng.*, **9**(4), 257-263.

Grilli, S.T., Skourup, J. and I.A., Svendsen (1989) "An efficient boundary element method for nonlinear water waves," *Engng. Analysis with Boundary Elements*, **6**(2), 97-107.

Grilli, S.T., Svendsen, I.A. and R., Subramanya (1997) "Breaking criterion and characteristics for solitary waves on slopes," *J. Waterway Port Coastal and Ocean Engng.*, **123**(3), 102-112.

Grilli, S.T. and R., Subramanya (1996) "Numerical modeling of wave breaking induced by fixed or moving boundaries," *Computational Mech.*, **17**, 374-391.

Grilli, S.T., Subramanya, R., Svendsen, I.A. and J., Veeramony (1994) "Shoaling of solitary waves on plane beaches," *J. Waterway Port Coastal and Ocean Engng.*, **120**(6), 609-628.

Guignard, S. and S.T., Grilli. (2001)"Modeling of shoaling and breaking waves in a 2D-NWT by using a spilling breaker model," *Proc. 11th Offshore and Polar Engng. Conf.* (ISOPE01, Stavanger, N, 6/01), 116-123.

Kan, M., Kawamura, T., Kuwahara, K. (2001). "Numerical study of the sand movement around a cylindrical body standing on the sand," *JSME Intern. J. B-Fluids, Therm. Engr.*, **44**(3), 427-433.

Vittori, G., and Blondeaux, P. (1990) "Sand ripples under sea waves. Part 2. Finite-amplitude development," *J. Fluid Mech.*, **218**, 19-39.

Voropayev, S.I., Testik, F.Y., Fernando, H.J.S. and Boyer, D.L. (2002a) "Burial and scour around short cylinder under progressive shoaling waves," *Ocean Engineering* (in press).

Voropayev, S.I., Testik, F.Y., Fernando, H.J.S. and Boyer, D.L. (2002b) "Morphodynamics and cobbles behavior in and near the surf zone," *Ocean Engineering* (in press).

ACKNOWLEDGEMENT

This research was supported by the Office of Naval Research, under grant N-00014-01-10349 from the US Department of the Navy, Office of the Chief of Naval Research.